International Journal of Bioprinting

RESEARCH ARTICLE

Fabrication of 3D gel-printed β-tricalcium phosphate/titanium dioxide porous scaffolds for cancellous bone tissue engineering

Xulin Hu[1], Hu Li[1], Liang Qiao[2], Shuhao Yang[1], Haoming Wu[1], Chao Peng[1], Yamei Zhang[1], Hai Lan[1], Hua Yang[3]*, Kainan Li[1]*

[1]Clinical Medical College and Affiliated Hospital of Chengdu University, Chengdu University, Chengdu 610081, China

[2]The First Affiliated Hospital, and College of Clinical Medicine of Henan University of Science and Technology, Luoyang 471003, China

[3]West China School of Public Health of Sichuan University, Chengdu 610041, China

Abstract

Human bone is composed of cortical bone and cancellous bone. The interior portion of natural bone is cancellous with a porosity of 50%–90%, but the outer layer is made of dense cortical bone, of which porosity was not higher than 10%. Porous ceramics were expected to be research hotspot in bone tissue engineering by virtue of their similarity to the mineral constituent and physiological structure of human bone. However, it is challenging to utilize conventional manufacturing methods to fabricate porous structures with precise shapes and pore sizes. Three-dimensional (3D) printing of ceramics is currently the latest research trend because it has many advantages in the fabrication of porous scaffolds, which can meet the requirements of cancellous bone strength, arbitrarily complex shapes, and individualized design. In this study, β-tricalcium phosphate (β-TCP)/titanium dioxide (TiO_2) porous ceramics scaffolds were fabricated by 3D gel-printing sintering for the first time. The chemical constituent, microstructure, and mechanical properties of the 3D-printed scaffolds were characterized. After sintering, a uniform porous structure with appropriate porosity and pore sizes was observed. Besides, biological mineralization activity and biocompatibility were evaluated by *in vitro* cell assay. The results demonstrated that the incorporation of TiO_2 (5 wt%) significantly improved the compressive strength of the scaffolds, with an increase of 283%. Additionally, the *in vitro* results showed that the β-TCP/TiO_2 scaffold had no toxicity. Meanwhile, the adhesion and proliferation of MC3T3-E1 cells on scaffolds were desirable, revealing that the β-TCP/TiO_2 scaffolds can be used as a promising candidate for repair scaffolding in orthopedics and traumatology.

Keywords: **β**-tricalcium phosphate; Titanium dioxide; 3D printing; Porous scaffolds; Bone tissue engineering

***Corresponding author:**
Hua Yang (yangwawa19@163.com)
Kainan Li
(likainan1961cdfy@126.com)

Citation: Hu X, Li H, Qiao L, *et al*., 2023, Fabrication of 3D gel-printed β-tricalcium phosphate/titanium dioxide porous scaffolds for cancellous bone tissue engineering. *Int J Bioprint*. 9(2): 673. https://doi.org/10.18063/ijb.v9i2.673

Received: October 17, 2022
Accepted: November 02, 2022
Published Online: January 19, 2023

1. Introduction

The aging of population and an increase in life expectancy worldwide is accompanied by a surge of bone-associated diseases, including catagma, osteoporosis, and bone

tumors[1-3]. An increasing demand for bone transplantation and regeneration approaches is now a critical issue in orthopedics. Autologous bone and allografts are considered a convenient strategy for bone repair operation, but each has some drawbacks[3,4]. For instance, variable quality, limited availability, chronic donor site pain, and second surgery requirement restrict their extensive applications, rendering it vital to seek alternatives. Consequently, synthetic bone-graft scaffolds were developed to overcome the inherent limitations of autografts and allografts, thus attracting great interest in the orthopedic field[5,6].

The aim of bone tissue engineering is to regenerate damaged osseous tissue to its original state using bionic scaffolds[7], relying on scaffolds that act as a platform to motivate cells to adhere and spread with the ultimate goal of bone regeneration[8,9]. The bionic bone scaffolds must be porous, characterized by the interconnected penetrating structure and pore with different sizes to sustain the growth of osteoblasts and provide a venue for vascularization[7,10,11]. Three-dimensional (3D) printing technology opens up new opportunities for fabricating bone scaffolds with different extremely complex architectures and arbitrary shapes[12], which is quite challenging for irregular bone defects by customization. Other than synthetic bone grafting granulation used in the therapy of small bone defects[10], the 3D-printed porous scaffolds provide interconnected pores and mechanical integrity, which are promising attributes in the treatment of large segmental defects[13].

Various biomaterials including bio-ceramics[14], polymers and metal alloys, have been used to fabricate porous bone scaffolds[15]. Among the different, calcium phosphate, typically the β-tricalcium phosphate (β-TCP) and hydroxyapatite (HA)[16,17], is the most popular due to its excellent bioactivity and biocompatibility[18]. Since β-TCP and HA are the components of human bones, their osteoconduction and osteointegration are similar to the natural bone[19], and they have been applied in bone repair and reconstruction[20,21]. Several conventional routes have been adopted to fabricate porous β-TCP scaffolds. Tunable pore sizes and porosity can be attained using a space holder-assisted powder processing to fabricate β-TCP scaffolds, but uncontrolled shrinkage during sintering gives rise to the insufficient mechanical strength of scaffolds[22]. Gel casting, summarized as a stable gel network in a casting mold which is sintered to decompose, is able to prepare ceramic scaffolds with high porosity but low interconnectivity[23]. Another conventional pore-forming method, freeze casting, has been utilized to manufacture porous ceramic scaffolds since the 2000s[24]. The main shortcomings of freeze casting are the complexity of controllability and commonly low porosity with small pore size[25]. Nevertheless, the aforementioned strategies cannot provide a controllable design of the complex shape as well as a microporous structure with precise parameters. Nowadays, 3D printing technology, combining computer-aided design (CAD) with computer-aided manufacturing (CAM), has been developed to manufacture porous structures with desirable porosity, precise shape, and adjustable pore size[26-28]. Furthermore, 3D printing is a promising technique for fabricating orthopedic implants for tissue engineering by virtue of customizable manufacturing and controlled hierarchical structures[29,30].

Here, considering the advantages of β-TCP ceramic and 3D printing technology, we designed and fabricated a novel β-TCP/titanium dioxide (TiO_2) ceramic porous scaffold using a 3D gel-printing sintering for the first time. Since TCP is brittle and has low tenacity[31], the TiO_2, which is also supposed to act as a base for nucleation, was incorporated to improve the mechanical properties of scaffolds. Meanwhile, TiO_2 can promote the adhesion of bone cells with good biocompatibility[32,33]. The objective of this work was to explore the manufacturing process of β-TCP/TiO_2 ceramic porous scaffold with a systematic characterization. Additionally, we demonstrated the adhesion, proliferation, and metabolic activity of the MC3T3-E1cells on scaffolds to evaluate its potential in bone tissue engineering.

2. Materials and methods

2.1. Materials

β-TCP and TiO_2 powder were obtained commercially (Kunshan Technology, China). All the chemicals used in this work, including gelatin, polyvinyl alcohol, and biological reagent, were purchased from Aladdin Biochemical Technology Co., Ltd (Shanghai, China). Other organic solvents and reagents were analytically pure and purchased from Kelong Chemical Reagent Co., Ltd (Chengdu, China).

2.2. Preparation of β-TCP/TiO_2 slurry and β-TCP/TiO_2 ceramic

A stable slurry with the proper ratio of additives is fundamental to scaffold fabrication[34]. In this study, β-TCP ceramics containing different weight TiO_2 (1–5 wt%) were produced via a molding-sintering method. First, 4 g β-TCP powder, 1.8 mL gelatin solution (20 wt%), 0.2 mL PVA solution (20 wt%) and TiO_2 powder were added into a 5-mL beaker and stirred thoroughly to obtain a ceramic slurry. The ceramic slurry was then injected into a prepared cylindrical mold with a diameter of 8 mm and a height of 4 mm. Second, the ceramic billet was taken out quickly from the mold after solidification. For the purpose of preventing the deformation or collapse in the subsequent degrease sintering process, the ceramic billet was put into a

freeze dryer at -80°C for 24 h to remove moisture. Finally, the lyophilized ceramic billets were sintered in a muffle furnace (KSL-1400X-A1, Kejing, China) in the different heating curves for degreasing to obtain the β-TCP/TiO_2 ceramic sample. Hereafter, sintered ceramic samples with 1 wt%, 2 wt%, 3 wt%, 4 wt%, and 5 wt% of TiO_2 were labeled as β-TCP/1-TiO_2 ceramic, β-TCP/2-TiO_2, β-TCP/3-TiO_2 ceramic, β-TCP/4-TiO_2 ceramic, and β-TCP/5-TiO_2 ceramic, respectively.

2.3. Fabrication and 3D printing process of β-TCP/TiO_2 ceramic scaffolds

The ceramic slurry containing different weight ratios of β-TCP, TiO_2, gelatin, and PVA was aspirated into a syringe and added to the biological 3D printer (B Series, Guangzhou Maipu Regenerative Medical Technology Co., Ltd, China). The nozzle model used in this experiment was 22G (inner diameter was 400 μm) and the layer thickness of 3D printing was set to 0.4 mm. Other print parameters are as follows: printing speed = 30 mm/s; printing temperature = 50°C; return axis speed = 5 mm/s; return axis length = 2 mm; temperature of ice plate = -5°C; heating temperature of the nozzle = 50°C; and discharge speed = 20 mm/s. The printing process was performed according to the pre-designed scaffold model (10 × 10 × 10 mm) and the filling rates were set to 20%, 30%, and 40%, respectively. After printing, the printed porous scaffolds were immediately put into the freeze dryer for freeze-drying at -80°C for 24 h. Finally, the frozen printed scaffolds were sintered in the muffle furnace in an optimized heating curve to fabricate the β-TCP/TiO_2 porous scaffolds. Hereafter, the sample of sintered ceramic scaffolds with 1 wt%, 2 wt%, 3 wt%, 4 wt%, and 5 wt% of TiO_2 was labeled as β-TCP/1-TiO_2 scaffold, β-TCP/2-TiO_2 scaffold, β-TCP/3-TiO_2 scaffold, β-TCP/4-TiO_2, scaffold, and β-TCP/5-TiO_2 scaffold, respectively.

2.4. Composition analysis of β-TCP/TiO_2 ceramics and scaffolds

2.4.1. X-ray diffraction analysis (XRD)

X-ray diffraction analysis (XRD) of ceramics was detected using an X-ray diffraction analyzer (DX-2700B, Hao Yuan instrument co., Ltd, China). The β-TCP/TiO_2 ceramic was milled into powder subjected to transmission analysis by CuK α-radiation with a voltage of 40 kV, a current of 30 mA and a scanning angle range of 20°–80°.

2.4.2. Fourier infrared spectroscopy analysis (FIRS)

Nicolet 6700 infrared spectrometer (Thermo Fisher, USA) was used to identify the functional groups of the β-TCP/TiO_2 ceramic samples. One to two milligram ceramic was grilled in an agate mortar to powder with dried potassium bromide. Subsequently, the mixed powder was pressed into pieces on the tablet press and tested.

2.4.3. Thermogravimetric analysis

Thermo-grameter analysis (METTLER TOLEDO, USA) was carried out to verify the thermostability of β-TCP/TiO_2 ceramic. For each group of samples, 10 mg ceramic was loaded into the crucible and heated at 20°C–800°C with a heating rate was 10°C/min under a nitrogen atmosphere.

2.4.4. Scanning electron microscopy (SEM) microscopic analysis

The morphologies and microstructure of the ceramics and scaffolds were examined by a field emission scanning electron microscopy (Phenom pro, Netherlands) with a voltage of 10 kV. Before observation, the surface of the specimens was sprayed with a thin gold-plated layer.

2.5. Mechanical properties

The mechanical properties of ceramic and scaffolds were carried out using a universal testing machine (SANSCMT4503, YinFei Electronic Technology Co., Ltd, China) at room temperature. For each ceramic or scaffold specimen, the samples were prepared into cylindrical ceramic sheets with a diameter of 8 mm and a height of 4 mm for compressive strength testing. The surface under the pressure was flat and there were no defects on the sample. The speed of the squeeze head was set at 1 mm/min with 4.8 kN force. Each group of ceramic plate samples was tested at room temperature with five parallel samples according to the compression test standard GBT 1964-1996.

2.6. Porosity of porous ceramic scaffolds

The inner porosity of ceramic scaffolds (10 × 10 × 10 mm) was also conducted using ethanol as a medium employing the Archimedean principle. The scaffold of each specimen was measured using a vernier caliper to determine the volume *V'*. The sample was immersed in ethanol in the sealed test tube. After 24 h, the differential of the liquid level of alcohol was denoted as *h,* and the change in the volume was denoted as *V.* At last, the r porosity of the ceramic scaffold was obtained by the following formula:

$$P = \left(1 - \frac{V}{V'}\right) \times 100\%, \quad V = \frac{\pi d^2}{4} \bullet h \tag{I}$$

Afterward, mean values and standard deviations were calculated from five specimens.

2.7. Biocompatibility evaluation of β-TCP/TiO_2 scaffolds

2.7.1. Bioactivity on biologic mineralization of β-TCP/TiO_2 scaffolds

The bioactivity of the β-TCP/TiO_2 ceramic scaffolds was evaluated by immersing them in a simulated body fluid (SBF) at 37°C for 14 days. After removing from the given solution, the formation of bone-like apatite and the chemical composition of deposits was characterized

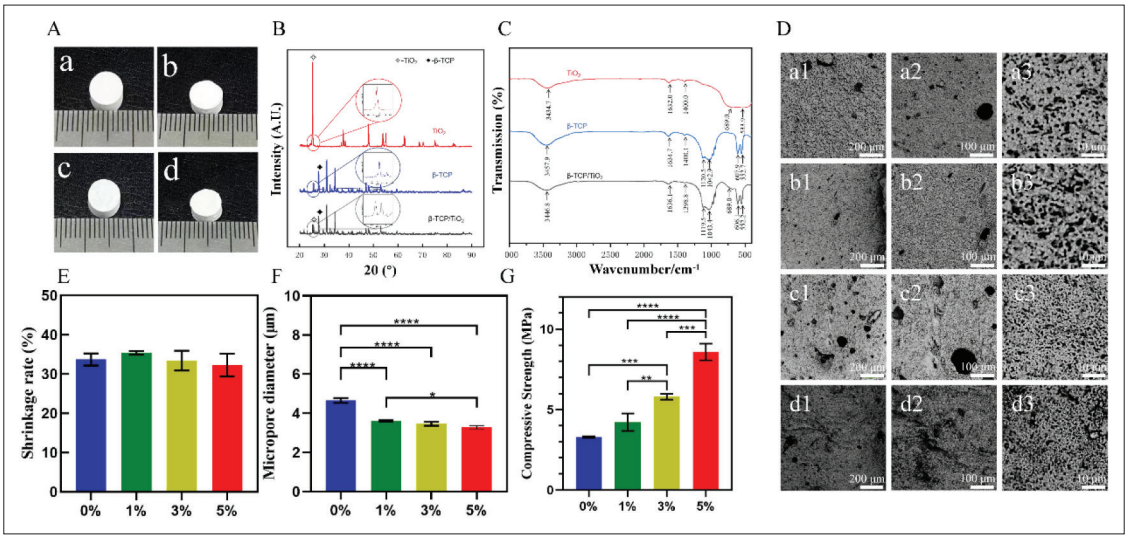

Figure 1. (A) Ceramic samples of β-TCP (a), β-TCP/1-TiO_2 (b), β-TCP/3-TiO_2 (c), and β-TCP/5-TiO_2 (d). (B) XRD diagram of TiO_2, β-TCP, and β-TCP/5-TiO_2 ceramic and details of the XRD diagram of the figure at 24.5°–26.5°. (C) Infrared spectrum of TiO_2, β-TCP, and β-TCP/5-TiO_2 ceramic. (D) Micromorphology of β-TCP/TiO_2 ceramics detected by SEM: β-TCP/TiO_2 (a), β-TCP/1-TiO_2 (b), β-TCP/3-TiO_2 (c), and β-TCP/5-TiO_2 (d). (E) The shrinkage of β-TCP/TiO_2 ceramic samples with 0% TiO_2, 1% TiO_2, 3% TiO_2 and 5% TiO_2. (F) Average diameter of micropores of β-TCP and β-TCP/TiO_2 ceramics. (G) The compressive strength of β-TCP and β-TCP/TiO_2 ceramics with different TiO_2 content.

by field emission scanning electron microscopy (FE-SEM) equipped with energy dispersive spectroscopy (EDS).

2.7.2. Cell biocompatibility and proliferation of β-TCP/TiO_2 ceramic scaffolds

Samples of ceramic scaffolds were sterilized by gamma-ray diffraction and were put into a 96-well cell plate cultured with MEMα medium containing 1% penicillin and streptomycin. 1 mL of mouse preosteoblast cells (MC3T3-E1) at a density of 6000 cells/well were seeded in each well and then cultured in a CO_2 incubator at 37°C for 1 and 3 days. After each incubation period, specimens were rinsed twice with phosphate-buffered saline, and then 10 μL MTT (5 mg/mL) was added to each well and incubated for another 3 h. The cell viability was detected by the optical density value, and the cell survival rate was counted.

The cells on the scaffold surface were stained and observed to investigate the proliferation and adhesion of osteoblasts on scaffolds. Briefly, after the end of each incubation period of 1, 3, and 7 days, osteoblasts were fixed in 5% paraformaldehyde and subjected to gradient dehydration using 30%, 50%, 80%, 90%, and 100% alcohol, followed by SEM observation. Meanwhile, after 1, 3, and 7 days of incubation in a cell incubator, the osteoblasts on scaffolds were also dyed with calcein AM/propidium iodide (PI) solution, and the adhesion of cells on the surface was observed by an inverted fluorescence microscope (Nikon Eclipse Ti-E, Japan).

2.8. Statistical analysis

All statistical data were calculated by Origin 2018 and GraphPad Prism 8. One-way analysis of variance (ANOVA) was conducted (**** $P < 0.0001$; *** $P < 0.001$; ** $P < 0.01$; * $P < 0.05$; NS, no significant difference).

3. Results and discussion

3.1. Characterization, morphology, and mechanical property of β-TCP/TiO_2 ceramic

Figure 1B revealed the XRD diagram of TiO_2, β-TCP and β-TCP/5-TiO_2 ceramic in detail. The XRD diffraction pattern of TiO_2 showed that the typical phase structure of the rutile phase, confirmed by the JCPDS card (21-1276) at 25.25°, 37.96°, 48.20°, 54.143°, and 62.87°[35]. The prominent peak of TiO_2 was found in the XRD diagram of β-TCP/5-TiO_2, indicating that rutile TiO_2 existed in the structure of β-TCP/5-TiO_2 ceramic. Besides, the addition of TiO_2 slightly affected the diffraction pattern of β-TCP in the range in diffraction angle from 25° to 25.5°, indicating that TiO_2 was indeed incorporated into the β-TCP matrix.

The infrared spectrum of TiO_2, β-TCP and β-TCP/TiO_2 ceramic is shown in Figure 1C. The vibration absorption peak of PO_4^{3-} was close to 1120 cm^{-1}, 1042cm^{-1}, 607cm^{-1}, and 552cm^{-1}[36]. Briefly, 1120 cm^{-1} and 1042 cm^{-1} belonged to the asymmetric stretching vibration of the P=O group; 607 cm^{-1} was the symmetric stretching vibration peak of PO_4^{3-}; 552 cm^{-1} corresponded to the bending vibration absorption. For TiO_2 particle, characteristic absorption

peak formed at 689 cm^{-1} and 533 cm^{-1}[37]. As expected, the characteristic peak of TiO_2 appeared distinctly in the infrared spectrum of β-TCP/5-TiO_2 ceramic powder. Therefore, TiO_2 was uniformly distributed and well-bound to the β-TCP matrix.

Figure 1A showed that the surface of ceramic samples was smooth without apparent cracks, but the volume of samples shrank because the ceramics became more compact after sintering. The volume shrinkage rate is depicted in Figure 1E. The average volume shrinkage rate of the sintered β-TCP ceramic was 33.73%. By contrast, the volume shrinkage rate of β-TCP/TiO_2 ceramic with different content of TiO_2 (1–5 wt%) were 35.38%, 33.42%, and 32.29%, respectively. The results showed that the addition of TiO_2 had little effect on the densification of β-TCP during sintering.

Micromorphologies of β-TCP/TiO_2 ceramics with different TiO_2 contents were detected by SEM (Figure 1D). A few large holes were seen in all the ceramic billets because in the process of sintering (scale plate in 200 μm), crystal water, PVA, and gelatin volatilized, causing a shrinkage of the ceramic volume. Nevertheless, the migration of the ceramic moving phase cannot fill the position of volatile matter, leading to the generation of a porous interior structure and large voids on the surface. Further observation in magnification (scale plate in 10 μm) revealed that ceramic grains were tightly packed and arranged to form some micropores. As implantation materials, these micropores were conducive to the adhesion of cells, facilitating the entry of nutrients and the expulsion of harmful metabolite[38]. To our satisfaction, the average diameter of micropores of β-TCP and β-TCP/TiO_2 ceramics reflected that the average pore size gradually decreased with the addition of TiO_2 (Figure 1F). In addition, the uniform distribution of cavities in different sizes also confirmed the excellent dispersion in ceramic slurry, which played a vital role in the subsequent biological 3D printing[39].

The compressive strength of β-TCP/TiO_2 ceramics is indicated in Figure 1G. The compressive strength of β-TCP/TiO_2 ceramics increased by 283%, from 3.30 MPa to 8.59 MPa, which meets the mechanical requirements of bone repair scaffolds. Thus, the introduction of TiO_2 significantly improved the mechanical performance of β-TCP and overcame shortcomings of the fragility of β-TCP ceramics. This may be due to two reasons: first, the addition of TiO_2 promotes the densification degree of ceramics to a certain extent; second, TiO_2 may also promote the crystallization of β-TCP, rendering the binary ceramic strong.

3.2. Printability of 3D β-TCP/TiO_2 scaffolds

The printability of 3D β-TCP/TiO_2 scaffolds is affected by the content and particle size of inorganic salts, PVA concentration, and temperature. While designing the printing ink formula, we choose gelatin with good biocompatibility as the main mobile phase because its temperature-sensitive characteristics could help with molding. Therefore, in this part, we mainly explored the influence of different inorganic salt addition and PVA solution addition on printability and formability of the stent (Figure 2). We found that the increase of inorganic salt content made ink extrusion difficult, but the addition of PVA component can effectively improve this problem. Therefore, in subsequent experiments, we chose 5% PVA as one of the ingredients in the printing ink formula.

3.3. Characterization of 3D β-TCP/TiO_2 scaffolds

Samples of β-TCP/TiO_2 ceramics scaffolds in different filling rates were presented with perforative pipelines, and interpenetrating pores were perceived in the ceramic scaffolds. The square pore structure was neatly arranged, and the pore diameter was uniform (Figure 3A). It showed that the size of cavities inside the ceramic scaffold increased gradually with a decrease in the filling rate. Similarly, when the filling rate was 40%, the average macropore diameter decreased to 0.25 mm (Figure 3D). As illustrated in Figure 3C, with filling rates of 20%, 30%, and 40%, the average porosity of the 3D scaffolds was 79.32%, 66.34%, and 62.49%, respectively. A higher filling rate often results in compact structures and a higher utility rate of space[40], which was in line with the result obtained in this work that the average porosity decreased with the increase of the filling rate.

The average shrinkage rates of β-TCP/3-TiO_2 scaffolds with filling rates of 20%, 30%, and 40% were 56.51%, 54.96%, and 53.57%, respectively (Figure 3B). According to the data, as the filling rate increased, the average shrinkage rates decreased slightly. Filling rates were another factor of the compressive strength of scaffolds (Figure 3E). The strength of the β-TCP/5-TiO_2 ceramics scaffolds was 0.81 MPa, 1.87 MPa, and 2.69 MPa, respectively, with 20%, 30%, and 40% filling rates. It can be concluded that when the content of TiO_2 was 5 wt%, a higher filling rate in the preparation process contributed to higher compressive strength of the scaffolds.

The appearance of β-TCP/TiO_2 ceramics scaffolds with different TiO_2 content is presented in Figure 4A. TiO_2 exhibited no effects affecting the appearance and internal structure of the scaffolds. No collapse and surface defects were found after the introduction of TiO_2, but alteration of void morphology was detected. The mean micropore diameter of β-TCP/TiO_2 ceramics scaffolds was 3 μm, which was a bit shorter than the micropore diameter in β-TCP scaffolds (Figure 4B). On the other hand, the content of TiO_2 had a negligible role on the porosity of β-TCP/TiO_2

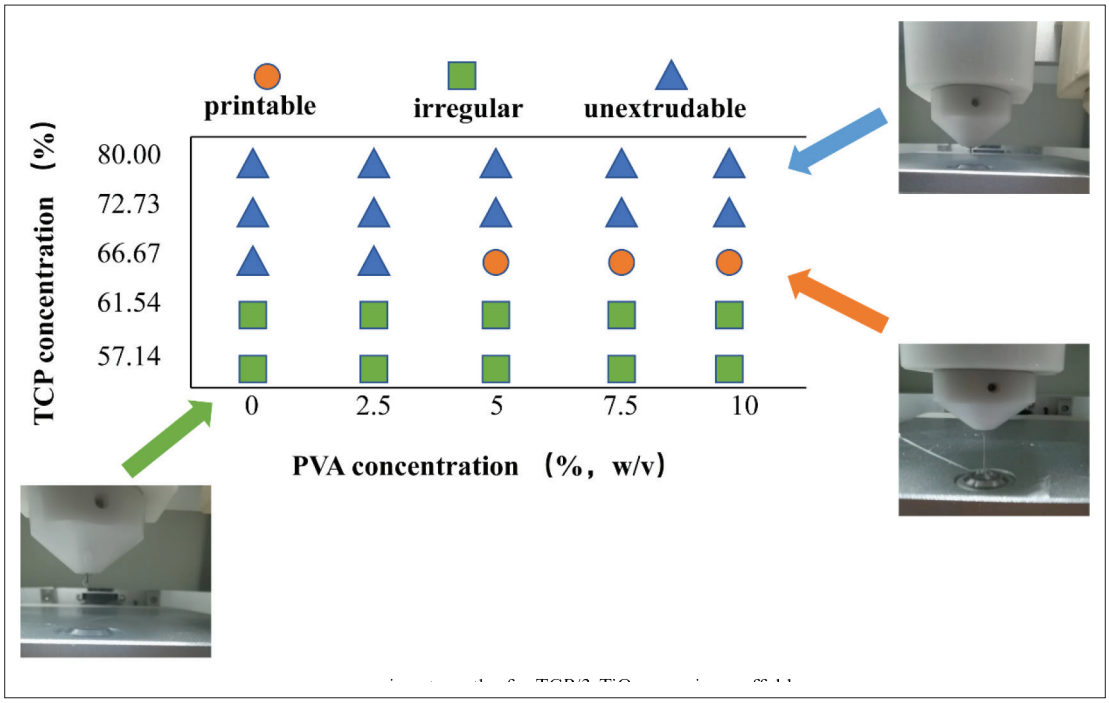

Figure 2. Printability in the fabrication of β-TCP/TiO_2 scaffolds

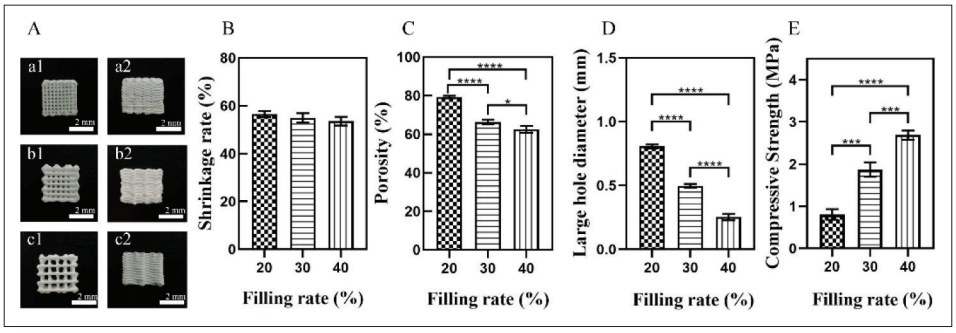

Figure 3. (A) Samples of β-TCP/3-TiO_2 ceramics scaffolds in different filling rates (a1 and a2: stents with a filling rate of 40%; b1 and b2: stents with a filling rate of 30%; c1 and c2: stents with a filling rate of 20%). (B) Effect of different filling rates on the shrinkage of β-TCP/3-TiO_2 scaffolds. (C) Effect of different filling rates on the porosity of β-TCP/3-TiO_2 scaffolds. (D) Average macropore diameter of β-TCP/3-TiO_2 ceramics scaffolds in different filling rate. (E) Effects of different filling rates on the compressive strength of β-TCP/3-TiO_2 ceramics scaffolds.

ceramics scaffolds (Figure 4D) because the average porosity of β-TCP/TiO_2 ceramics scaffolds was on a scale of 65.55%–66.39%. Similarly, TiO_2 content has little effect on the shrinkage of β-TCP/TiO_2 porous ceramic scaffold (Figure 4E). Thus, it was concluded that the addition of TiO_2 filler was unable to change the formation mechanism and crystallization-molding process of ceramic sintering. The average shrinkage rates of β-TCP/3-TiO_2 scaffolds with filling rates of 20%, 30%, and 40% were 56.51%, 54.96%, and 53.57%, respectively (Figure 6). According to the data, as the filling rate increased, the average shrinkage rates decreased slightly.

The mechanical properties of bone repair scaffolds play a crucial role in healing bone defects. For β-TCP/TiO_2 ceramics scaffolds, the compressive strength of β-TCP ceramics scaffold was 0.35 MPa (Figure 4C). After the incorporation with TiO_2, the compressive strength of the ceramics gradually increased to 0.72 MPa.

3.4. Morphologies of 3D β-TCP/TiO_2 scaffolds

The SEM images of β-TCP/TiO_2 porous ceramic scaffolds with different TiO_2 contents, showing surface and cross-section of the scaffolds (Figure 5), were used to investigate the morphology and microstructure of scaffold sintered at 1100°C. The whole structure of β-TCP and β-TCP/TiO_2 scaffolds was intact without apparent defects and cracks on the surface (Figure 5A). We noticed that the surface of the scaffold was even and smooth without cracks, and the interconnection between layers was glossy (scale

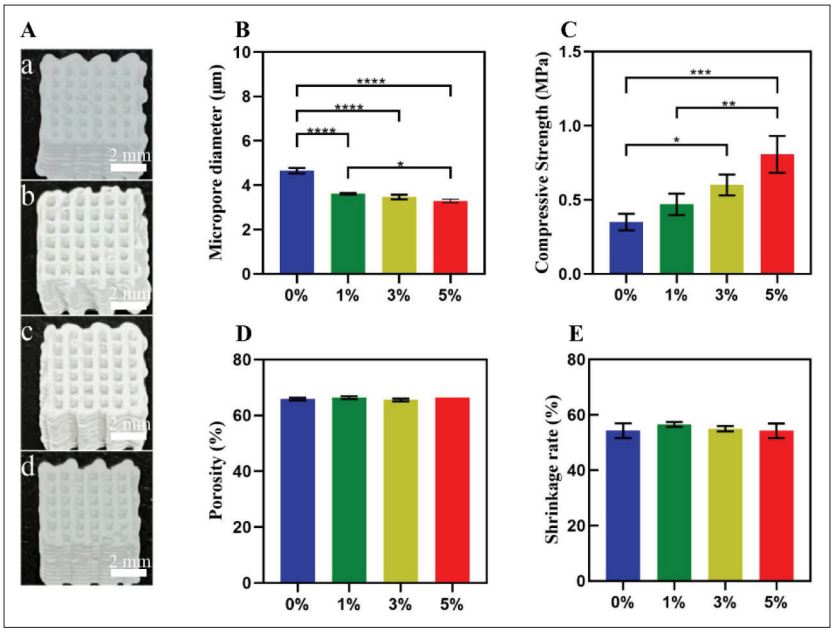

Figure 4. (A) Appearance of β-TCP/TiO_2 ceramics scaffolds with different TiO_2 content. (B) Mean micropores diameter of β-TCP and β-TCP/TiO_2 ceramics scaffolds. (C) The compressive strength of β-TCP and β-TCP/TiO_2 ceramics scaffolds with different TiO_2 content. (D) Effect of different TiO_2 content on the porosity of β-TCP/ TiO_2 ceramics scaffolds with a filling rate of 30%. (E) Effect of different TiO_2 content on the shrinkage of β-TCP/TiO_2 ceramics.

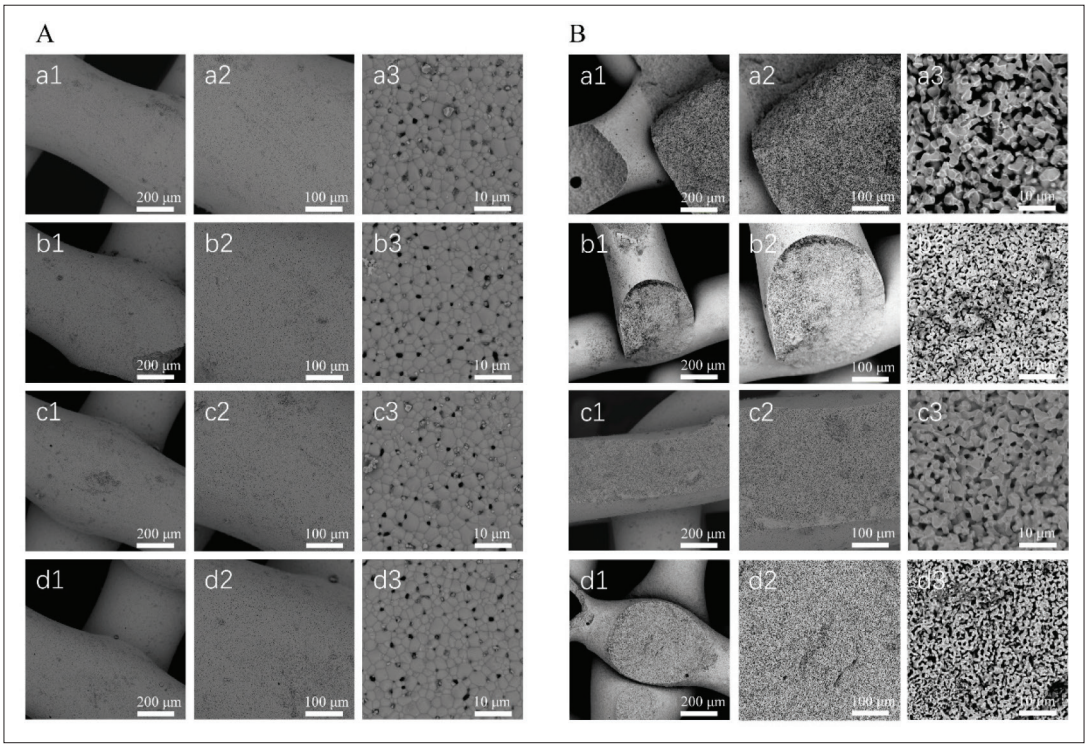

Figure 5. Micromorphology of β-TCP/TiO_2 ceramics scaffolds detected by SEM. (A) Outward surface. (B) Fracture surface. Groups a, b, c, and d are ceramic scaffolds with 0% TiO_2, 1% TiO_2, 3% TiO_2, and 5% TiO_2 components, respectively. Groups a1, b1, c1, and d1 are visualized by SEM with 300× magnification; scale bar: 200 μm. Groups a2, b2, c2 and d2 are visualized by SEM with 600× magnification; scale bar: 100 μm. Groups a3, b3, c3, and d3 are visualized by SEM with 6000× magnification; scale bar: 10 μm.

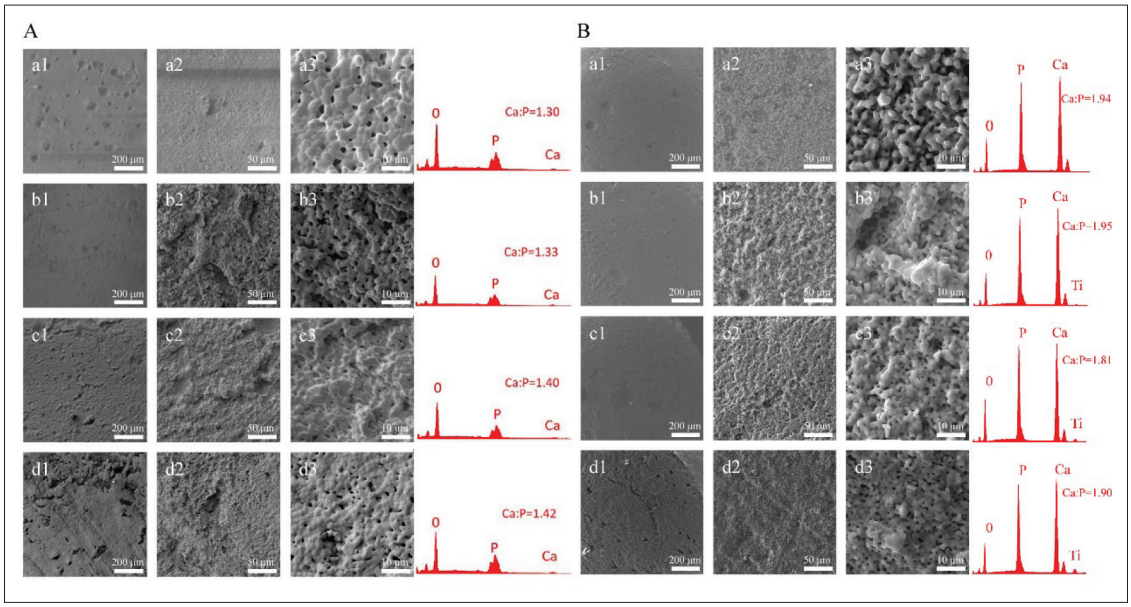

Figure 6. Scanning energy spectrum of β-TCP/TiO_2 ceramic scaffolds after 28 days (A) and 14 days (B) of biomineralization. Groups a, b, c, and d show the mineralization of ceramic scaffolds with 0% TiO_2, 1% TiO_2, 3% TiO_2, and 5% TiO_2 components, respectively. Groups a1, b1, c1, and d1 are visualized by SEM with 75× magnification; scale bar: 200 μm. Groups a2, b1, c2, and d2 are visualized by SEM with 300× magnification; scale bar: 50 μm. Groups a3, b3, c3, and d3 are visualized by SEM with 1500× magnification; scale bar: 10 μm.

plate in 200 μm). Furthermore, on account of adequate liquidity and no slurry agglomeration in the 3D printer nozzle, the ceramic slurry was evenly distributed without phase separation. The sintered ceramic scaffolds were constituted by pyknotic crystalline grain (scale plate in 10 μm). As is well-known, regulable micropores promote the degradation and mineralization of implant materials in the body[39]. Moreover, dense micropores were also uniformly distributed on the surface of scaffolds, positively influencing bone regeneration in an indirect fashion. Micromorphologies of β-TCP/TiO_2 ceramics scaffolds, implying the cross-section, are displayed in Figure 5B. There were evenly distributed micropores inside the beams of scaffolds, which provide a pathway for the exchange of metabolism and nutrients between cells and external environment, thus promoting proliferation and differentiation of osteoblasts.

3.5. Biological mineralization of β-TCP/TiO_2 scaffolds

The formation of an apatite layer on the implant material surface is the key step to inducing good bone healing[41]. Biomineralization is a crucial index to manifest formation process and mechanism of biological minerals[42]. Therefore, the bone-bonding ability of bioactive material is often assessed by examining the apatite-forming ability on its surface in SBF. The calcium-phosphorus ratio of tricalcium phosphate was 1.5[43]. After being immersed in SBF for 14 days, the Ca/P ratio of ceramic scaffolds of four groups (β-TCP: 1.94, β-TCP/1-TiO_2: 1.95, β-TCP/3-TiO_2: 1.81, and β-TCP/5-TiO_2: 1.90) was higher than that of tricalcium phosphate (Figure 6A). This suggested that β-TCP stimulated calcium and phosphorus ions to form a hydroxyapatite layer on scaffolds in the SBF. Scanning energy spectrum of the β-TCP/TiO_2 ceramic scaffold after 14 days of biomineralization demonstrated that for all the ceramic scaffolds, the light intensity of calcium and phosphorus elements was far higher than that of oxygen and titanium elements (Figure 6B). Since the calcium and phosphorus elements were enriched on the surface of the scaffold, the β-TCP/TiO_2 ceramic scaffolds fabricated in this work had excellent biological mineralization ability and were possible to promote the growth of bone *in vivo*.

3.6. Cell biocompatibility and proliferation

To better understand the cell proliferation and migration on β-TCP/TiO_2 scaffolds, an MTT assay was carried out using MC3T3-E1 osteoblasts after being cultured (Figure 7A). Compared to the blank control (CK) group, the cell viability of cells on the ceramic scaffold was approximately 130%–140%, much higher than CK group after being cultured for 24 h. After 72 h of incubation, the cell viability decreased as a result of the normal apoptosis. It is worth noting that the cell viability was still higher than the value of the CK group. Although TiO_2 has been reported to promote the growth of osteoblasts, this experiment did not improve the proliferation of MC3T3-E1 cells. In summary, the β-TCP/TiO_2 ceramic

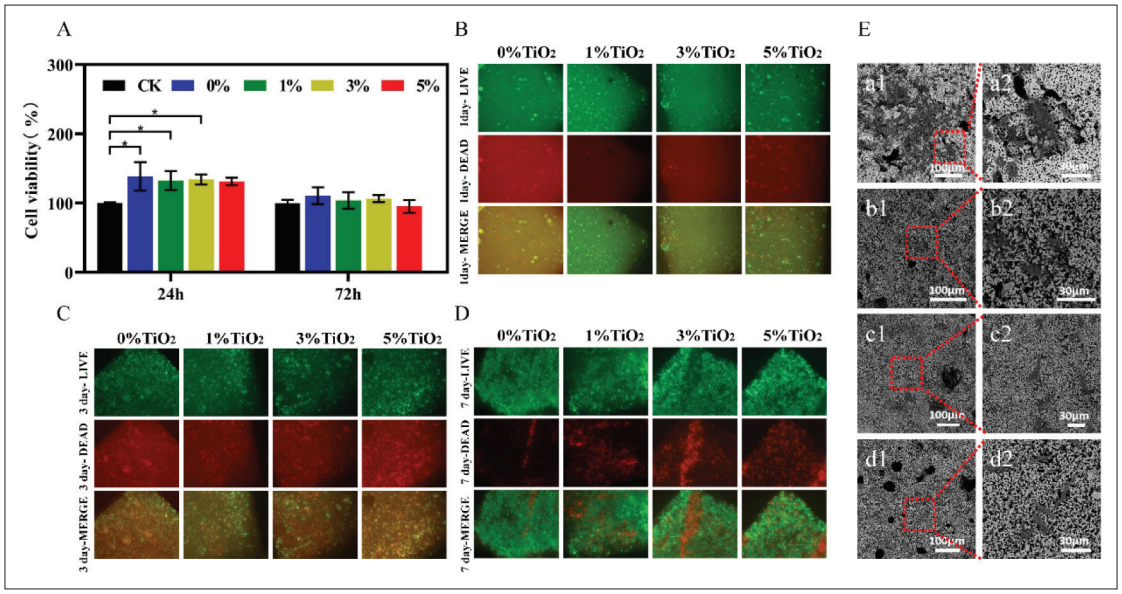

Figure 7. (A) The MTT assay results showing cell viability rate of MC3T3-E1 osteoblasts cultured on β-TCP/TiO_2 ceramic scaffolds with different content of TiO_2 (CK was the blank control group). (B) Osteoblast fluorescence detection of MC3T3-E1 cells on β-TCP/TiO_2 ceramic scaffolds for 1, 3, and 7 days. (C) Osteoblast fluorescence detection of dead MC3T3-E1 cells on β-TCP/TiO_2 ceramic scaffolds for 1, 3, and 7 days. (D) Corresponding osteoblast fluorescence detection of living/dead cells of MC3T3-E1 cells on β-TCP/TiO_2 ceramic scaffolds after 7 days of incubation. (E) Cell morphologies of MC3T3-E1 osteoblast cells cultured on β-TCP/TiO_2 ceramic scaffolds: β-TCP/TiO_2 (a), β-TCP/1-TiO_2 (b), β-TCP/3-TiO_2 (c), and β-TCP/5-TiO_2 (d).

scaffold has no cytotoxicity and stimulates cell growth. Besides, all scaffolds were verified to have a similar outcome of cell viability in the MTT assay. The results also confirmed that β-TCP/TiO_2 ceramic scaffolds have good biocompatibility and cytocompatibility.

Cell fluorescence staining was examined to observe the cell proliferation and adhesion of osteoblast cells on the surface of β-TCP/TiO_2 scaffolds (Figure 7B). Despite only a small number of MC3T3-E1 cells adhering to the ceramic scaffolds after 1 day of incubation, osteoblasts cells proliferated rapidly on 3 and 7 days. After 1 day of culture, the cells on the scaffolds increased rapidly on 3 and 7 days. Notably, it was perceived that the living cells covered almost the surface of scaffolds. Figure 7C demonstrates that dead cells on β-TCP/TiO_2 ceramic scaffolds increased simultaneously during cell culture. Therefore, the state of cell adhesion, growth, and proliferation on scaffolds was favorable. Furthermore, by comparing the distribution of the living and dead osteoblasts on 7 days, we found that the number of living cells was significantly higher than that of dead cells (Figure 7D). Figure 7E shows the morphology of MC3T3-E1 cells on the surface of β-TCP/TiO_2 ceramic scaffolds. MC3T3-E1 cells proliferated well with a stretched cell shape on the scaffolds. Besides, due to the abundant micropores on the surface, the cells adhered to the scaffolds firmly. To sum up, the β-TCP/TiO_2 ceramic scaffold has good cytocompatibility and was conducive to the growth of osteoblast cells.

4. Conclusion

The present work demonstrated the fabrication of β-TCP/TiO_2 ceramic porous scaffolds for bone tissue engineering using a 3D gel-printing sintering for the first time. The shrinkage ratio with filling rates of 20%, 30%, and 40% was 56.51%, 54.96%, and 53.57%, respectively. The porosity of the sintered scaffolds ranged from 65.55% to 66.39%, and the high porosity was conducive to cell proliferation and nutrient delivery. The compressive strength of the β-TCP ceramics scaffold was 0.35 MPa. After TiO_2 was incorporated, the compressive strength of the ceramics increased to 0.72 MPa, which meets the requirements of cancellous bone.

After immersion in SBF for weeks, the Ca/P ratio on the surface of ceramics scaffolds increased, implying the formation of a bone-like apatite layer and bioactivity. Furthermore, the *in vitro* study demonstrated that both the β-TCP scaffold and β-TCP/TiO_2 porous scaffolds were favorable for cell adhesion, growth and proliferation of MC3T3-E1 osteoblast cells. In conclusion, the β-TCP/TiO_2 porous scaffold has a lot of potential to be a promising bone repair scaffold in craniomaxillofacial and orthopedics surgery.

Acknowledgments

None.

Funding

This work was supported by Generation method and application verification of personalized rehabilitation prescription for patients with balance (2019YFB1311403); Natural Science Foundation of Sichuan Province-(23NSFSC5880); Chengdu Medical Research Project (2022004); Natural Science Foundation of Clinical Medical College and Affiliated Hospital of Chengdu University

Conflict of interest

The authors declare no conflict of interest.

Author contributions

Conceptualization, supervision, investigation, formal analysis, writing original draft, writing - Xulin Hu
Review and editing - Hu Li
Methodology, writing – review & editing - Liang Qiao, Shuhao Yang
Writing – review & editing, Investigation - Haoming Wu, Chao Peng
Investigation - Yamei Zhang, Hai Lan, Hua Yang
Conceptualization, Methodology, Resources - Kainan Li

Ethics approval and consent to participate

Not applicable.

Consent for publication

All agree to publish.

Availability of data

The data presented in this study are available on request from the corresponding author.

References

1. Ribas RG, Schatkoski VM, Do Amaral Montanheiro TL, *et al.*, 2019, Current advances in bone tissue engineering concerning ceramic and bioglass scaffolds: A review. *Ceram Int*, 45(17):21051–21061.
2. Brunello G, Sivolella S, Meneghello R, *et al.*, 2016, Powder-based 3D printing for bone tissue engineering. *Biotechnol Adv*, 34(5):740–753.
3. Salhotra A, Shah HN, Levi B, *et al.*, 2020, Mechanisms of bone development and repair. *Nat Rev Mol Cell Biol*, 21(11):696–711.
4. Palmer S, Gibbons C, Athanasou N, 1999, The pathology of bone allograft. *J Bone Joint Surg Br,* 81(2):333–335.
5. Meißner R, Bertol L, Rehman MAU, *et al.*, 2019, Bioprinted 3D calcium phosphate scaffolds with gentamicin releasing capability. *Ceram Int,* 45(6):7090–7094.
6. Mohan N, Palangadan R, Fernandez FB, *et al.*, 2018, Preparation of hydroxyapatite porous scaffold from a 'coral-like' synthetic inorganic precursor for use as a bone substitute and a drug delivery vehicle. *Mater Sci Eng C*, 92:329–337.
7. Ravanbakhsh H, Luo Z, Zhang X, *et al.*, 2022, Freeform cell-laden cryobioprinting for shelf-ready tissue fabrication and storage. *Matter*, 5(2):573–593.
8. Amini AR, Laurencin CT, Nukavarapu SP, 2012, Bone tissue engineering: Recent advances and challenges. *Crit Rev Biomed Eng*, 40(5):363-408.
9. Salgado AJ, Coutinho OP, Reis RL, 2004, Bone tissue engineering: State of the art and future trends. *Macromol Biosci*, 4(8):743–765.
10. Moore WR, Graves SE, Bain GI, 2001, Synthetic bone graft substitutes. *ANZ J Surg*, 71(6):354–361.
11. Hu X, Zhao W, Zhang Z, *et al.*, 2023, Novel 3D printed shape-memory PLLA-TMC/GA-TMC scaffolds for bone tissue engineering with the improved mechanical properties and degradability. *Chin Chem Lett*, 34(1):107451.
12. Lu J, Hu X, Yuan T, *et al.*, 2022, 3D-printed poly (P-dioxanone) stent for endovascular application: In vitro evaluations. *Polymers*, 14(9):1751.
13. Hu X, Lin Z, He J, *et al.*, 2022, Recent progress in 3D printing degradable polylactic acid-based bone repair scaffold for the application of cancellous bone defect. *MedComm Biomater Appl*, 1(1):e14.
14. Ghahsareh ZS, Banijamali S, Aghaei A, 2022, Cerium oxide containing canasite based glass-ceramics for dental applications: Crystallization behavior, mechanical and chemical properties. *Ceram Int*, 48(6):8489–8501.
15. Chen Q, Thouas GA, 2015, Metallic implant biomaterials. *Mater Sci Eng R*, 87:1–57.
16. Li Y, Xie K, Wang C, *et al.*, 2021, 3D printing of tricalcium phosphate/poly lactic-co-glycolic acid scaffolds loaded with carfilzomib for treating critical-sized rabbit radial bone defects. *Int J Bioprint*, 7(4):405.
17. Zheng C, Attarilar S, Li K, *et al.*, 2021, 3D-printed HA15-loaded β-tricalcium phosphate/poly (lactic-co-glycolic acid) bone tissue scaffold promotes bone regeneration in rabbit radial defects. *Int J Bioprint*, 7(1):317.
18. Ma PX, 2008, Biomimetic materials for tissue engineering. *Adv Drug Delivery Rev*, 60(2):184–198.
19. Srinivasan B, Kolanthai E, Nivethaa E, *et al.*, 2022, Enhanced in vitro inhibition of MCF-7 and magnetic properties of cobalt incorporated calcium phosphate (HAp and β-TCP) nanoparticles. *Ceram Int*, 49(1):855–861.

20. Mofakhami S, Salahinejad E, 2021, Biphasic calcium phosphate microspheres in biomedical applications. *J Control Release*, 338:527–536.

21. Lobo SE, Arinzeh TL, 2010, Biphasic calcium phosphate ceramics for bone regeneration and tissue engineering applications. *Materials*, 3(2):815–826.

22. Deisinger U. Generating porous ceramic scaffolds: processing and properties; proceedings of the Key Engineering Materials, F, 2010 [C]. Trans Tech Publ. *Key Eng Mater*, 441:155–179

23. Wongwitwichot P, Kaewsrichan J, Chua K, *et al.*, 2010, Comparison of TCP and TCP/HA hybrid scaffolds for osteoconductive activity. *Open Biomed Eng J*, 4:279.

24. Shahrouzifar M, Salahinejad E, Sharifi E, 2019, Co-incorporation of strontium and fluorine into diopside scaffolds: Bioactivity, biodegradation and cytocompatibility evaluations. *Mater Sci Eng C*, 103:109752.

25. Macchetta A, Turner IG, Bowen CR, 2009, Fabrication of HA/TCP scaffolds with a graded and porous structure using a camphene-based freeze-casting method. *Acta Biomater*, 5(4):1319–1327.

26. Gbureck U, Hölzel T, Klammert U, *et al.*, 2007, Resorbable dicalcium phosphate bone substitutes prepared by 3D powder printing. *Adv Funct Mater*, 17(18):3940–3945.

27. Xu T, Zhao W, Zhu J-M, *et al.*, 2013, Complex heterogeneous tissue constructs containing multiple cell types prepared by inkjet printing technology. *Biomaterials*, 34(1):130–139.

28. Söhling N, Al Zoghool S, Schätzlein E, *et al.*, 2022, In vitro evaluation of a 20% bioglass-containing 3D printable PLA composite for bone tissue engineering. *Int J Bioprint*, 8(4):602.

29. Horn TJ, Harrysson OL, 2012, Overview of current additive manufacturing technologies and selected applications. *Sci Prog*, 95(3):255–282.

30. Yi S, Liu Q, Luo Z, *et al.*, 2022, Micropore-forming gelatin methacryloyl (GelMA) bioink toolbox 2.0: Designable tunability and adaptability for 3D bioprinting applications. *Small*, 18(25):2106357.

31. Baudín C, Benet T, Pena P, 2019, Effect of graphene on setting and mechanical behaviour of tricalcium phosphate bioactive cements. *J Mech Behav Biomed Mater*, 89:33–47.

32. Bakhtiyari SSE, Karbasi S, Monshi A, *et al.*, 2016, Evaluation of the effects of nano-TiO2 on bioactivity and mechanical properties of nano bioglass-P3HB composite scaffold for bone tissue engineering. *J Mater Sci Mater Med*, 27(1):1–17.

33. Ghasemi S, Ghomi H, 2021, Investigation of applying chitosan coating on antibacterial and biocompatibility properties of bredigite/titanium dioxide composite scaffolds. *J Biomater Appl*, 36(3):406–418.

34. Melchels FP, Domingos MA, Klein TJ, *et al.*, 2012, Additive manufacturing of tissues and organs. *Prog Polym Sci*, 37(8):1079–1104.

35. Naicker PK, Cummings PT, Zhang H, *et al.*, 2005, Characterization of titanium dioxide nanoparticles using molecular dynamics simulations. *J Phys Chem B*, 109(32):15243–15249.

36. Arsad MS, Lee PM, Hung LK, 2011, Synthesis and characterization of hydroxyapatite nanoparticles and β-TCP particles. *Proceedings of the 2nd International Conference on Biotechnology and Food Science*, IPCBEE, F.

37. Peters RJ, Van Bemmel G, Herrera-Rivera Z, *et al.*, 2014, Characterization of titanium dioxide nanoparticles in food products: Analytical methods to define nanoparticles. *J Agric Food Chem*, 62(27):6285–6293.

38. Wu T, Yu S, Chen D, *et al.*, 2017, Bionic design, materials and performance of bone tissue scaffolds. *Materials*, 10(10):1187.

39. Chen Z, Li J, Liu C, *et al.*, 2019, Preparation of high solid loading and low viscosity ceramic slurries for photopolymerization-based 3D printing. *Ceram Int*, 45(9):11549–11557.

40. Shepherd J, Best S, 2011, Calcium phosphate scaffolds for bone repair. *JOM*, 63(4):83–92.

41. Miller C, Kokubo T, Reaney I, *et al.*, 2002, Formation of apatite layers on modified canasite glass–ceramics in simulated body fluid. *J Biomed Mater Res*, 59(3):473–480.

42. Li P, Ohtsuki C, Kokubo T, *et al.*, 1993, Process of formation of bone-like apatite layer on silica gel. *J Mater Sci Mater Med*, 4(2):127–131.

43. Gandolfi MG, Taddei P, Tinti A, *et al.*, 2011, Alpha-TCP improves the apatite-formation ability of calcium-silicate hydraulic cement soaked in phosphate solutions. *Mater Sci Eng C*, 31(7):1412–1422.